Black hole scalarization induced by the spin: 2 + 1 time evolution

Daniela D. Doneva[1,2,*] Lucas G. Collodel[1,†] Christian J. Krüger[1,‡] and Stoytcho S. Yazadjiev[1,3,4,§]

[1]*Theoretical Astrophysics, Eberhard Karls University of Tübingen, Tübingen 72076, Germany*
[2]*INRNE—Bulgarian Academy of Sciences, Sofia 1784, Bulgaria*
[3]*Department of Theoretical Physics, Faculty of Physics, Sofia University, Sofia 1164, Bulgaria*
[4]*Institute of Mathematics and Informatics, Bulgarian Academy of Sciences, Acad. G. Bonchev St. 8, Sofia 1113, Bulgaria*

(Received 26 August 2020; accepted 7 October 2020; published 9 November 2020)

Scalarization is a very interesting phenomenon allowing a compact object to be endowed with scalar hair while leaving all the predictions in the weak field limit unaltered. In Gauss-Bonnet gravity, the source of the scalar field can be the curvature of the spacetime. It was recently shown that for a particular type of coupling function between the scalar field and the Gauss-Bonnet invariant, spin-induced black hole scalarization is possible. In the present paper, we study this phenomenon by performing a $2+1$ time evolution of the relevant linearized scalar field perturbation equation and examine the region where the Kerr black hole becomes unstable, giving rise to new scalarized rotating black holes. This is a direct numerical approach to study the development of spin-induced scalarization, and it can serve as an independent check of previously published results.

DOI: 10.1103/PhysRevD.102.104027

I. INTRODUCTION

Alternative theories of gravity play a major role in the research performed by relativists and cosmologists around the globe, even while general relativity (GR) keeps thriving with its predictions as new ways of probing it are developed. Two main reasons support this practice. The first is our current understanding of the large scale structure of the Universe based on observations, which requires the existence of a weakly interacting matter field known as dark matter, yet not experimentally found, as well as a negative pressure field which we call dark energy, capable of producing the late time accelerated expansion, and also a similar field named inflaton, which would have caused the early inflationary period of our Universe. The second reason is that GR is a classical nonrenormalizable theory that is expected to break down at the Planck scale, and therefore cannot tell the whole story. In exploring different theories, one may not ignore the success achieved by GR so far; hence, any deviations from it on classical scales are assumed to take place at the strong regime, i.e., in the vicinity of a compact object such as a black hole. Understanding what features to look for in such deviations and how they relate among different theories is key to better categorizing the whole myriad of generalizations found thus far in the literature.

In GR and several classes of scalar-tensor theories, the usual no-hair theorems apply; see, e.g., [1–5]. The exceptions are given by dropping the theorem's assumption that the matter fields share the same isometries of the spacetime, which allows for black holes with *synchronized hair* given by some complex spin-0 or spin-1 field endowed with a Noether charge that cannot be accessed asymptotically through the metric components [6–15]. Accordingly, the existence of hairy black holes greatly constrains the classes of theories which are serious contenders to expand GR's predictions.

Extensively studied is a special subset of Hordenski theories known as Einstein-dilaton-Gauss-Bonnet (EdGB) theory, where the general relativistic action is extended to include quadratic terms which are curvature invariant—the Gauss-Bonnet term $\mathcal{R}^2_{\rm GB}$. Such a term alone is a topological one which does not contribute to the dynamics in four spacetime dimensions, but in the EdGB theory, it is coupled to a scalar field through an exponential function $f(\varphi) = \alpha \exp(-\gamma\varphi)$ [16–20]. The dynamics of the dilatonic field is prescribed by a Klein-Gordon (KG) equation (plus Maxwell's equations when further coupled to an electromagnetic field) that does not allow for trivial (scalar hair free) solutions, due to the special form of the coupling. Therefore, dilatonic hair is featured in all solutions, and GR black holes are not part of them.

Recently, it has been realized that by modifying the coupling function it is possible to recover GR as a special set of the theory; in particular, if $df(\varphi)/d\varphi = 0$ for a certain constant φ_0, then $\varphi = \varphi_0$ everywhere is a possible

*daniela.doneva@uni-tuebingen.de
†lucas.gardai-collodel@uni-tuebingen.de
‡christian.krueger@tat.uni-tuebingen.de
§yazad@phys.uni-sofia.bg

 © 2020 American Physical Society

solutions to the KG equations. The scalar field no longer represents the dilaton, and this class is generally referred to as Einstein-scalar-Gauss-Bonnet theory (EsGB). This constraint on the coupling function is interesting for it leads to a *curvature-induced spontaneous scalarization* as noted for the first time for static black holes [21–23]. In short, around compact objects, the curvature becomes large enough to trigger the dynamics of the scalar field. Different objects have been studied in this class of theories—spherically symmetric black holes with different couplings and their stability properties [24–35]; scalarized neutron stars [22,36]; wormholes with no exotic matter [31]; particlelike solutions [37,38], which describe a scalar field divergent at the origin, but whose energy-momentum tensor is regular everywhere, and so is the spacetime. Rotating EsGB black holes, which are the topic of investigation of this article, have been reported in Refs. [39,40] for different coupling functions.

In this paper, we probe the stability of Kerr EsGB black holes by evolving in $2+1$ dimensions the modified Klein-Gordon equation describing the scalar perturbation of Kerr black holes within the EsGB gravity and determine in which regions of the parameter space that defines the theory a tachyonic instability gives rise to hairy black holes. We focus only on the case where the second order derivative of the coupling function has a negative sign that cannot lead to scalarization in the static case as in Refs. [21,22], but instead spin-induced scalarization is observed above a certain threshold of the black hole angular momentum. We note that a similar work has recently appeared in preprint versions [41], later supported by some analytical calculations [42], but it uses a different methodology where one decomposes the angular dependency of the scalar field onto a basis set of spherical harmonics and evolves the resulting system in $1+1$ dimensions. The present paper is meant to perform an independent check of the main results in Ref. [41] from a different perspective.

II. SCALAR FIELD PERTURBATIONS WITHIN GAUSS-BONNET GRAVITY

The action of Einstein-scalar-Gauss-Bonnet gravity in vacuum is given by

$$S=\frac{1}{16\pi}\int d^4x\sqrt{-g}[R-2\nabla_\mu\varphi\nabla^\mu\varphi+\lambda^2 f(\varphi)\mathcal{R}^2_{\rm GB}], \quad (1)$$

where, as usual, R is the Ricci scalar with respect to the spacetime metric $g_{\mu\nu}$, φ is the scalar field with coupling function $f(\varphi)$, λ is the Gauss-Bonnet coupling constant[1] having dimension of *length*, and $\mathcal{R}^2_{\rm GB}$ is the Gauss-Bonnet invariant, which is defined by $\mathcal{R}^2_{\rm GB}\coloneqq R^2-4R_{\mu\nu}R^{\mu\nu}+R_{\mu\nu\alpha\beta}R^{\mu\nu\alpha\beta}$ where $R_{\mu\nu}$ is the Ricci tensor and $R_{\mu\nu\alpha\beta}$ is the Riemann tensor. The action (1) yields the field equations

$$R_{\mu\nu}-\frac{1}{2}Rg_{\mu\nu}+\Gamma_{\mu\nu}=2\nabla_\mu\varphi\nabla_\nu\varphi-g_{\mu\nu}\nabla_\alpha\varphi\nabla^\alpha\varphi, \quad (2)$$

$$\nabla_\alpha\nabla^\alpha\varphi=-\frac{\lambda^2}{4}\frac{df(\varphi)}{d\varphi}\mathcal{R}^2_{\rm GB}, \quad (3)$$

where ∇_μ is the covariant derivative with respect to the spacetime metric $g_{\mu\nu}$ and $\Gamma_{\mu\nu}$ is defined by

$$\begin{aligned}\Gamma_{\mu\nu}\coloneqq&-R(\nabla_\mu\Psi_\nu+\nabla_\nu\Psi_\mu)-4\nabla^\alpha\Psi_\alpha\left(R_{\mu\nu}-\frac{1}{2}Rg_{\mu\nu}\right)\\&+4R_{\mu\alpha}\nabla^\alpha\Psi_\nu+4R_{\nu\alpha}\nabla^\alpha\Psi_\mu\\&-4g_{\mu\nu}R^{\alpha\beta}\nabla_\alpha\Psi_\beta+4R^\beta{}_{\mu\alpha\nu}\nabla^\alpha\Psi_\beta\end{aligned} \quad (4)$$

with

$$\Psi_\mu\coloneqq\lambda^2\frac{df(\varphi)}{d\varphi}\nabla_\mu\varphi. \quad (5)$$

In what follows, we will consider asymptotically flat spacetimes and the case for which the cosmological value of the scalar field is zero, i.e., $\varphi_0=0$. Without loss of generality, we can impose the following constraints on the coupling function $f(\varphi)$: $f(0)=0$ and $\frac{d^2f}{d\varphi^2}(0)=\epsilon$ with $\epsilon=\pm1$. Since the focus of the present paper is on spontaneous scalarization, we impose one more condition on $f(\varphi)$, namely, $\frac{df}{d\varphi}(0)=0$, which is crucial for the spontaneous scalarization. Under this condition, it is not difficult to see that the Kerr black hole solution is also a solution to EsGB gravity with trivial scalar field $\varphi=0$. As in the nonrotating case, the question that arises is whether the Kerr solution is stable within the framework of the bigger EsGB theory. Of course, the stability, in general, depends on the parameters of the Kerr solution, i.e., its mass M and angular momentum a as well as on the Gauss-Bonnet coupling parameter λ.

In order to study the stability of the Kerr black hole, we shall consider the perturbation of the Kerr solution within the framework of EsGB gravity. It is not difficult to see that when the coupling function satisfies the condition $\frac{df}{d\varphi}(0)=0$, the equations governing the perturbations of the metric $\delta g_{\mu\nu}$ are decoupled from the equation governing the perturbation $\delta\varphi$ of the scalar field. The equations for metric perturbations are in fact the same as those in the pure Einstein gravity, and therefore we shall focus only on the scalar field perturbations. The equation governing the scalar perturbation, assuming that $\frac{df}{d\varphi}(0)=0$, clearly does not depend on the exact form of the coupling function $f(\varphi)$ but instead only on the sign of the second derivative $\frac{d^2f}{d\varphi^2}(0)$ and is given by

[1]Note that λ is connected to the parameter η used in Ref. [41] in the following way: $\lambda^2=4\eta$.

$$\Box_{(0)}\delta\varphi + \frac{\epsilon}{4}\lambda^2\mathcal{R}^2_{\mathrm{GB}(0)}\delta\varphi = 0, \tag{6}$$

where $\Box_{(0)}$ and $\mathcal{R}^2_{\mathrm{GB}(0)}$ are the d'Alembert operator and the Gauss-Bonnet invariant for the background Kerr geometry.

As discussed in the Introduction, the Gauss-Bonnet invariant can act as a source for the scalar field and lead to black hole scalarization. For this to happen, the entire coefficient of $\delta\varphi$ (containing $\mathcal{R}^2_{\mathrm{GB}(0)}$) in Eq. (6) needs to take positive values in a certain region of the parameter space. This is clearly possible for $\epsilon = 1$ that leads to scalarization of both static and rotating black holes recently discovered in Refs. [21,22]. If $\epsilon = -1$, though, the term can remain positive if $\mathcal{R}^2_{\mathrm{GB}(0)}$ is greater than zero in a certain region outside the black hole. This is possible only for the rotating Kerr solution as we will demonstrate below. Thus, in the present paper, we will focus only on the latter case, i.e., $\epsilon = -1$.

In standard Boyer-Lindquist coordinates, the Kerr metric is written as

$$ds^2 = -\frac{\Delta - a^2\sin^2\theta}{\Sigma}dt^2 - 2a\sin^2\theta\frac{r^2 + a^2 - \Delta}{\Sigma}dtd\phi + \frac{(r^2+a^2)^2 - \Delta a^2\sin^2\theta}{\Sigma}\sin^2\theta d\phi^2 + \frac{\Sigma}{\Delta}dr^2 + \Sigma d\theta^2, \tag{7}$$

where $\Delta \coloneqq r^2 - 2Mr + a^2$ and $\Sigma \coloneqq r^2 + a^2\cos^2\theta$. The Gauss-Bonnet invariant for the Kerr solution is explicitly given by

$$\mathcal{R}^2_{\mathrm{GB}(0)} = \frac{48M^2}{\Sigma^6}(r^2 - a^2\cos^2\theta) \times (r^4 - 14a^2r^2\cos^2\theta + a^4\cos^4\theta). \tag{8}$$

Before writing down the explicit form of the perturbation equation (6), we introduce a new azimuthal coordinate ϕ_* defined by

$$d\phi_* \coloneqq d\phi + \frac{a}{\Delta}dr. \tag{9}$$

Working with ϕ_* allows us to get rid of some unphysical pathologies near the horizon. Furthermore, it is convenient to replace the radial coordinate r by the tortoise coordinate x, which is given by

$$dx \coloneqq \frac{r^2 + a^2}{\Delta}dr. \tag{10}$$

In the coordinates (t, x, θ, ϕ_*), the perturbation equation (6) takes the explicit form

$$\begin{aligned} &-[(r^2+a^2)^2 - \Delta a^2\sin^2\theta]\partial_t^2\delta\varphi + (r^2+a^2)^2\partial_x^2\delta\varphi + 2r\Delta\partial_x\delta\varphi - 4Mar\partial_t\partial_{\phi_*}\delta\varphi \\ &\quad + 2a(r^2+a^2)\partial_x\partial_{\phi_*}\delta\varphi + \Delta\left[\frac{1}{\sin\theta}\partial_\theta(\sin\theta\partial_\theta\delta\varphi) + \frac{1}{\sin^2\theta}\partial^2_{\phi_*}\delta\varphi\right] \\ &= \lambda^2\frac{12M^2\Delta}{\Sigma^5}(r^2 - a^2\cos^2\theta)(r^4 - 14a^2r^2\cos^2\theta + a^4\cos^4\theta)\delta\varphi. \end{aligned} \tag{11}$$

For large enough a, there exists a region of the spacetime outside the black hole in which the right-hand side takes negative values, which can potentially lead to scalarization. While the right-hand side is always exactly zero at the horizon (as it contains a factor of Δ), several negative local minima appear in its vicinity as one approaches the poles, $\theta = 0$ and $\theta = \pi$. A necessary condition for the right-hand side to assume negative values is $a/M > 0.5$, and the negative minima get more pronounced as a is increased. However, the existence of such negative minima close to the poles is only a necessary but not a sufficient condition for modes of the Kerr black hole to become unstable and thus for scalarization. Based on the analysis of the scalarization in the nonrotating case [21,22], though, one can expect that scalarization will develop more quickly with larger values of a and the subsequent increase of the negative part of the term in the right-hand side. Indeed, the numerical simulations confirm this expectation as we will see in the following sections.

III. NUMERICAL METHOD

A. Numerical approach

Equation (11) is clearly an analog of the Klein-Gordon equation with variable squared mass proportional to the Gauss-Bonnet invariant. Even though this new term is responsible for very important phenomenology, i.e., the destabilization of the Kerr solution and the appearance of scalarized hairy black holes, it does not pose additional challenges from a numerical point of view. Therefore, we can use the same approach as has been used for the numerical solution of the standard wave and Klein-Gordon equation. As mentioned in the Introduction, our approach is to directly evolve the perturbation equation (11) in time, which, after separating out the azimuthal dependence, has only two spatial dimensions. We can perform this separation since the background is axisymmetric and we are considering only small perturbations on this background. Thus, we decompose the perturbation of the scalar field $\delta\varphi$ according to

$$\delta\varphi(t,x,\theta,\phi_*) = \delta\tilde{\varphi}(t,x,\theta)e^{im\phi_*}, \tag{12}$$

where m is an integer (the well-known azimuthal mode number), and our code will solve for the variable $\delta\tilde{\varphi}$. After substituting the above decomposition into Eq. (11), the ϕ_*-derivative will be replaced by a simple multiplication with im, i.e., $\partial_{\phi_*} \to im$. This allows us to select a particular value for m for any simulation.

A step further was taken in Ref. [41] (see also Refs. [43,44]), in which the angular dependence of the perturbation function $\delta\varphi$ was expanded in series of the spherical harmonics that makes it possible to separate modes with different l number. Since we are dealing with perturbations on a rotating background, it is not possible to rigorously attribute a particular value of l to a specific mode as modes of different l couple to each other. Nevertheless, experience shows that even for rapid rotation, it is possible to define with a good accuracy l-led modes, which in the Schwarzschild limit, i.e., $a = 0$, reduce to the corresponding nonrotating modes[2] with the same l (see, e.g., Refs. [45,46]). This approach has the advantage that it is easier to separate the behavior for different l and even to study the coupling between the different modes due to rotation. When solving Eq. (11), though, one is inevitably limited to a finite number of spherical harmonics in the expansion of $\delta\varphi$. Modes of lower order l are normally those that are more prone to instabilities; i.e., such a treatment of the problem is physically justified and will generally yield accurate results.

For this paper, we have opted for the time evolution approach in order to investigate the threshold for destabilization of the Kerr solutions. When evolving the $2+1$ version of the modified Teukolsky equation, it is possible, after properly choosing the initial data, to separate well the different l modes only in the nonrotating case where they decouple. As soon as rotating black holes are considered, the mode coupling causes excitation of modes with different l, and it is expected that the $l = |m|$ mode will have the dominant contribution at late times if we limit ourselves to stable modes (see, e.g., Ref. [47]). As far as unstable modes are concerned, the mode that is "most unstable" (meaning that it has the shortest growth time) for a fixed m and for all l will eventually dominate the signal.

B. Code implementation

The direct solution of the $2+1$ Teukolsky equation for different spins was performed in Refs. [48–52]. In addition, the modified Klein-Gordon equation in Chern-Simons gravity was considered in Ref. [47], in which the destabilization of the Kerr black hole was shown to appear for a certain range of parameters. There are various sophisticated numerical techniques and analytical transformations that can be applied in order to cure different numerical issues such as instabilities caused by the appearance of first order derivative in time or the reflection at the outer boundary. It turns out, though, that most of these problems are missing in our case or can be easily avoided. For example, in the modified Klein-Gordon equation (11), no instabilities due to first order time derivatives are present, unlike the Teukolsky equation with a spin different from zero [49].

We are evolving Eq. (11) in time, assuming the decomposition of the scalar field given in Eq. (12). The numerical scheme is similar to the one considered in Refs. [53,54] for the evolution of spacetime perturbations around rotating neutron stars: we use finite differences of second order to approximate spatial derivatives, while we perform the time integration using a third order Runge-Kutta method. Further, we have to impose boundary conditions at the edges of the numerical grid: both at the outer edge of the grid, being preferably as "far away" as possible, and at the inner edge, located very close to the event horizon, we impose usual outgoing wave boundary conditions (also known as the Sommerfeld boundary condition [55]) in order to remove energy from the grid that reaches those boundaries. Truncation errors will inevitably lead to undesired reflections from the outer boundary. One possibility to prevent the reflected wave from spoiling the extracted signal is to push the outer boundary of the numerical grid sufficiently far away, such that the spurious reflection returns to the location at which the signal is extracted only after a time such that the unspoiled signal has a long enough duration for a satisfactorily precise analysis. At the rotation axis, i.e., for $\theta = 0$ and $\theta = \pi$, the boundary conditions are less involved. As we are dealing with scalar perturbations, the scalar field has to be zero along the rotation axis when $m > 0$; for $m = 0$, we require its θ-derivative to vanish to ensure smoothness of the solution.

Our simulations are performed on a grid that is uniform in the tortoise coordinate x. The computational domain in radial direction spans the interval $[r_+ + \varepsilon_r, r_\infty]$, where ε_r is a small shift away from the outer horizon radius r_+, where the coordinate system would become singular, and r_∞ denotes the radius of the grid at its outer edge; this interval is mapped to the tortoise coordinate domain $[x_{-\infty}, x_{+\infty}]$. The outgoing wave boundary conditions at the radial edges of the computational grid are independent of the polar angle θ; we impose $(\partial_t \pm \partial_x)\delta\varphi = 0$ at the boundaries, where the sign is chosen depending on whether we consider the inner or the outer boundary. The numerical implementation of these boundary conditions is inspired by the derivation given in Ref. [56].

For the majority of the simulations, we employ a grid with 500×60 points in x and θ directions, while for the coordinate x, our grid spans the interval $[-20, 50]$. The observer is located at $x = 30$. Our results show that this choice yields an error of usually less than 0.5% in the

[2]In the nonrotating case, modes with different value of l are decoupled, and thus it is possible to rigorously attribute an l number to each mode.

determination of the growth time of the unstable models, while the threshold values of the parameters where the instability develops has an accuracy of over 99.9%. The main reason why we have chosen such moderate accuracy and value of x_∞ is that some of the plots require running several thousands of simulations and the chosen parameters lead to a good balance between computational expense and accuracy.

For initial data, we take a perturbation which has the shape of a Gaussian in radial direction, located at roughly $x_{\rm Gauss} = 12$ and with width $\sigma_{\rm Gauss} = 1$. For the θ-dependence of the initial data, we take that of a spherical harmonic of order l. In the nonrotating case where no mode coupling is present, such initial data excite to very good accuracy predominantly modes with this specific m and l. For rotating black holes, there will be mixing and thus excitation of modes with different values of l. It turns out, though, that, at least as far as stable solutions are considered, the corresponding l-led mode will normally have the largest amplitude and thus dominate the signal.

The oscillation frequencies are extracted by performing a Fourier transform of the time signal. The frequency determination is inevitably spoiled by somewhat larger errors due to the rather limited number of oscillations before the asymptotic tail appears; the number of oscillations we observe can be as low as 2–3 in the case of initial data with $l = 0$ (i.e., $l = 0$-led modes) but increases rapidly with larger values of l, thus leading to improved accuracy of the extracted frequencies. The damping times are extracted by matching the peaks of the oscillation modes with an exponential function that is also prone to larger errors when a smaller number of peaks is present in the signal.

It is clear that Eq. (11) can be scaled with the black hole mass M and thus the x-coordinate, the frequencies, and the parameter λ are measured in units of M (in our numerical implementation, we set $M = 1$). Our calculations are performed in such dimensionless units.

IV. RESULTS

A. Reliability of the numerical code

We have performed various tests in order to confirm the correctness and to study the accuracy of the code we have developed. The first and most natural one is to calculate the quasinormal mode (QNM) frequencies of Schwarzschild and Kerr black holes. QNMs with specific l and m can be excited by simply adopting the θ-dependence of the corresponding spherical harmonic in the initial data, while m is a parameter of our evolution equation. Our results show that the obtained oscillation frequencies and damping times of Schwarzschild and Kerr black holes are in agreement with the ones available in the literature (see, e.g., Refs. [57,58]) with an error typically up to a few percent that decreases for higher l.

For a next step, we have tried to confirm the results for the instabilities in Chern-Simons gravity [47]. We have successfully reproduced the instability line to very good accuracy, i.e., the threshold combination of a and the Chern-Simons parameter $\eta_{\rm CS}$ where the modes start to grow exponentially with time.

Last but not least, we have tested the behavior of the code against different resolutions and dependence on the auxiliary parameters, such as the distance of the outer edge of the grid from the black hole and the width and location of the initial Gaussian pulse. We have verified numerically that the relevant quantities, such as the frequencies and the damping/growth time of the modes, indeed converge to specific values when increasing the resolution. The distance of the outer edge of the grid from the black hole has no impact on the accuracy of the observed waveforms, but instead it spoils the signal after a certain amount of time when the spurious reflection from the grid's outer edge reaches the location of signal extraction. Therefore, low values of $x_{+\infty}$ will effectively lead to a significant reduction of the number of clear oscillation cycles observed. This is not the case, though, for unstable modes whose instability typically develops rapidly; thus, the outer edge of the grid can be safely chosen to be closer to the black hole than in simulations in which we need a longer evolution time for the extraction of proper waveforms of the stable modes.

B. Instabilities of the scalar field perturbations

Due to the scalar field's harmonic dependence on the azimuthal coordinate, only the azimuthal mode number m enters the perturbation equation explicitly. Thus, for unstable models, the exponential growth will be dominated by the fastest growing mode for a fixed m irrespective of the initial perturbation. We have checked this explicitly, and indeed the mode growth time is independent of the number l of the initial perturbations.

In Fig. 1 (left panel), we show the behavior of the axisymmetric (i.e., $m = 0$) scalar field perturbation observed at $x = 30$ for $a/M = 0.8$ and three different values of λ starting from pure GR with $\lambda = 0$. In order to show the time evolution of the stable mode in the pure GR case up until the appearance of the asymptotic tail (i.e., up to $t/M \gtrsim 250$), we have performed these simulations on a computational grid that extends much farther away from the black hole than in most of the other simulations, while keeping the radial resolution constant. More specifically, we used 2500×60 points in x and θ directions, respectively, and the outer edge of the grid was located at $x_{+\infty} = 250$. Across all our simulation, the initial data we use for $\delta\varphi$ have different values of l for the different m; however, as previously stated, this has relevance only for stable modes or for the few oscillations before the onset of the exponential growth of the mode for higher λ. For these simulations, we have set $m = 0$; hence, the superradiant instability is suppressed which implies that the exponential

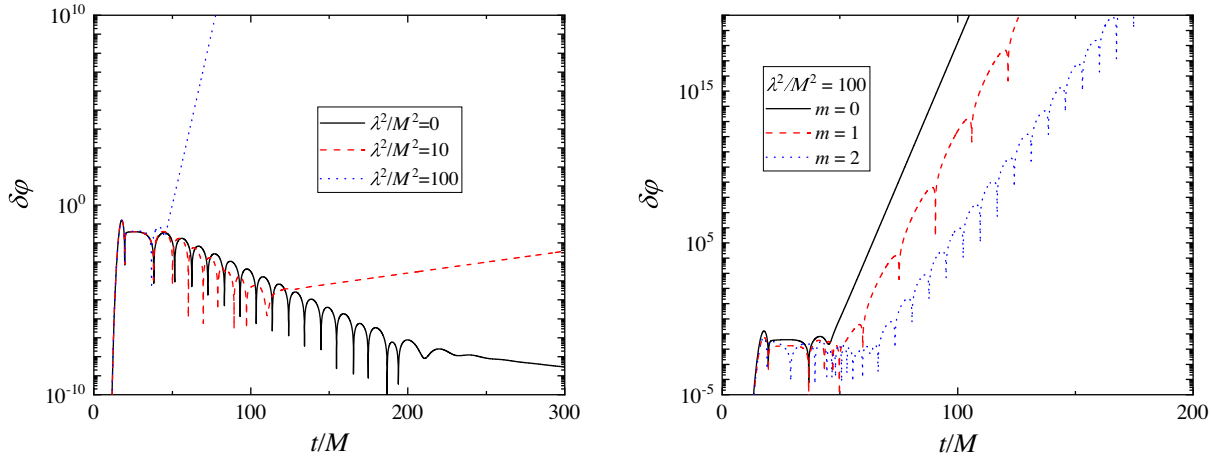

FIG. 1. The time evolution of $\delta\varphi$ as observed at $x = 30$ for $m = 0$ and three different values of λ (left panel) and $\lambda^2/M^2 = 100$ and three different values of m (right panel). The dimensionless angular moment is chosen to be $a/M = 0.8$.

growth is solely due to the instabilities linked to the scalarization. As one can see from the figure, increasing the parameter λ leads to a shorter growth time τ of the mode (which is defined to be the e-folding time of the growth of the scalar perturbation); in other words, a larger coupling constant λ results in a more rapid development of the instability.

The qualitative change of the signal for different m is depicted in the right panel of Fig. 1. As one can see, during the exponential growth for $m = 0$, no oscillations are present after the onset of the instability. This is due to the fact that $m = 0$ is a special case for which the real and the imaginary parts of Eq. (11) decouple.[3] This is not the case for $m > 0$ where the coupling between the real and imaginary parts of $\delta\varphi$ leads to oscillations even in the exponentially growing part of the time signal (similar considerations but within the Chern-Simons gravity can be found in Ref. [47]). From this figure, it is also visible that the growth time increases with increasing m. This gives us the confidence to believe that the $m = 0$ case leads to the shortest growth times and, subsequently, it is the most relevant one for the instabilities.

A contour plot of the growth times for $m = 0$, which is supposed to be the subset of modes with the shortest growth times, is shown in Fig. 2. We plot the thresholds for the appearance of unstable Kerr solutions for $m = 0$, 1, 2 (the solid, dashed, and dotted lines, respectively); it is evident that for fixed angular momentum a, the instabilities develop only for larger values of λ as m is increased. In addition, it is apparent that with increasing λ, the threshold value of a above which scalarization may occur seems to saturate for all three values of m. This is expected since, as we have mentioned in Sec. II, the potential in the evolution equation for the scalar field may take negative values only for $a/M > 0.5$. An advantage of our code concerning the instability studies is that only the azimuthal number m is an input parameter. Therefore, if a mode of large l is susceptible to the instability, it will eventually develop and cause the perturbation of the scalar field to grow exponentially in our time evolution. However, we do observe numerical instabilities in our code when evolving the perturbations for very large λ^2/M^2 of the order of 10^4–10^5; we are able to overcome those instabilities by increasing the grid resolution even though we are eventually limited by computational expense. Additionally, when we pick a combination of angular momentum a and coupling constant λ which is very close to the threshold of instability, the growth or damping time of the modes

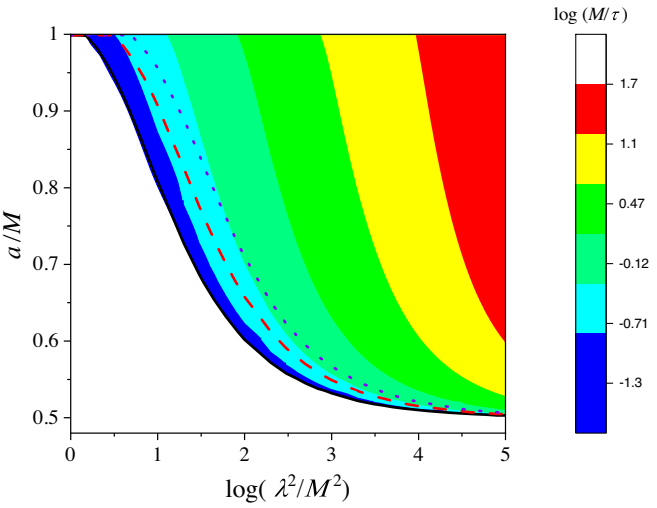

FIG. 2. A contour plot of the growth time of the unstable modes for $m = 0$. In addition, the threshold lines, i.e., the contour lines $a(\lambda)$ dividing the parameter space into stable and unstable regions, are plotted with solid black line for $m = 0$, with a dashed red line for $m = 1$ and with a dotted purple line for $m = 2$.

[3]Real and imaginary $\delta\varphi$ can be introduced because of the substitution (12) that results in a double number of equations for the real $\delta\varphi_R$ and the imaginary $\delta\varphi_I$.

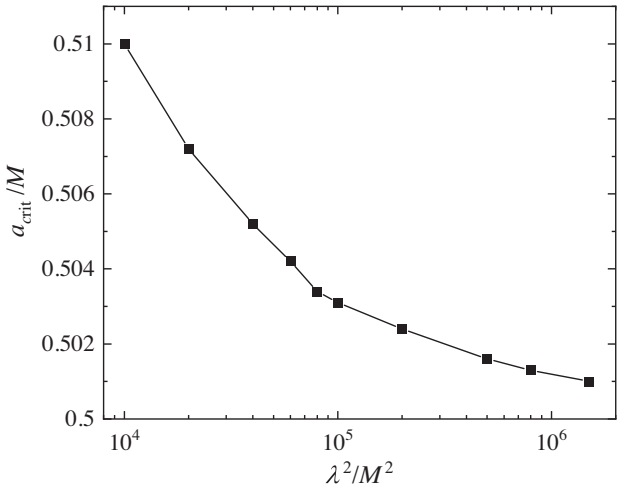

FIG. 3. The critical value of $a_{\rm crit}$ (for $m = 0$) as a function of λ^2/M^2 above which the instability is present. Only the region for very large $\lambda^2/M^2 \gtrsim 10^4$ is shown, which is corresponding to the bottom-left corner of Fig. 2.

becomes very large, and subsequently we need a very long evolution in order to check for instabilities. This makes the accurate determination of the threshold line for large values of λ even more challenging.

In our simulations, we reached up to $\lambda^2/M^2 \sim 10^6$, and we discovered that the critical value of the angular momentum for the onset of instability fell below $a_{\rm crit}/M \sim 0.501$. The dependence of $a_{\rm crit}$ as a function of λ^2 (for very large λ) is shown in Fig. 3; it is evident that with the increase of the coupling parameter, $a_{\rm crit}$ decreases and apparently saturates. For the computation of the points in Fig. 3 corresponding to the largest values of λ, we had to increase the grid resolution by a factor of 5 in both the x and θ directions in order to avoid numerical instabilities, resulting in a correspondingly larger computational expense. These results are in agreement within the numerical accuracy with Ref. [41] and the analytical considerations in Ref. [42], in which a threshold value of $a_{\rm crit}/M = 0.5$ in the $l \to \infty$ limit was argued.

Apart from the value of $a_{\rm crit}/M$, we have performed a comparison between the numerical values of τ inside the instability region produced with our code and in Ref. [41]. Naturally, the results in Ref. [41] were presented only in the form of a contour plot, and thus extracting exact numerical values of τ is difficult. In addition, we used the coupling parameter λ similar to that in Ref. [21] that is connected to the parameter η used in Ref. [41] in the following way $\lambda^2 = 4\eta$. After taking all this into account, it turned out that our results for τ/M are in a very good agreement with those in Ref. [41], within the numerical accuracy.

Summarizing, despite the severe numerical instabilities that appear in our simulations for large values of λ, the $2 + 1$ calculations seem to be in good agreement with the $a_{\rm crit}/M = 0.5$ limit derived in Ref. [42]. Another independent check of $a_{\rm crit}$ would be the construction of the actual equilibrium rotating scalarized solutions, but stationary solutions near critical points might be very challenging to obtain numerically.

V. CONCLUSIONS

In the present paper, we have considered the $2 + 1$ time evolution of the linearized scalar field perturbation equation in Gauss-Bonnet gravity. We are working with a subclass of theories having a negative second order derivative of the scalar field coupling function that can lead to spin-induced black hole scalarization as shown in Refs. [41,42]. In this case and when $a/M > 0.5$, there is a region in the vicinity of the black hole horizon and the rotation axis where the Gauss-Bonnet term, which appears in the perturbation equation for the scalar field, changes sign and hence the effective two-dimensional potential will have negative values. In comparison to previous numerical studies, we are performing a time evolution in two spatial dimensions without assuming any particular θ dependence. This approach is more direct and has the advantage that the time signal is completely independent of the l number and depends only on the azimuthal mode number m. Thus, it serves as in independent check of the studies presented in Refs. [41,42].

The developed numerical code is tested against different particular cases, such as the QNMs of Kerr black holes and the similar development of instabilities in Chern-Simons gravity. The code showed a good behavior when studying different resolutions, extents of the numerical grid, and shapes of the initial Gaussian pulse. A general feature of the signal for unstable modes of black holes with large spin parameter a is that, after a few damped oscillations, the amplitude of the scalar field perturbation starts to grow exponentially. For marginally unstable modes, the evolution time needed to observe the development of this instability might increase significantly, and in addition those simulations require high resolution to overcome numerical instabilities.

We have studied the instability region for $m = 0, 1, 2$ on a $a - \lambda$-diagram, where λ is the Gauss-Bonnet coupling constant. Our results show that, as expected, the $m = 0$ perturbations are the most relevant for the instability; i.e., they lead to the largest instability window. Naturally, the growth time of the unstable modes is shorter for larger a, and for every λ, above a certain threshold, there exists a critical angular momentum $a_{\rm crit}/M$ above which the Kerr black hole is unstable within the Gauss-Bonnet theories. With increasing λ, the critical angular momentum $a_{\rm crit}/M$ saturates. Despite the numerical difficulties encountered in the simulations for very large values of λ, we have managed to reach $a_{\rm crit}/M = 0.501$ for $\lambda^2/M^2 = 4 \times 10^6$. This is in agreement with the derived limit $a > 0.5$, where a negative minimum of the effective potential appears, and coincides within the numerical error with the results in Refs. [41,42].

ACKNOWLEDGMENTS

D. D. and L. C. acknowledges financial support via an Emmy Noether Research Group funded by the German Research Foundation under Grant No. DO 1771/1-1. D. D. is indebted to the Baden-Wurttemberg Stiftung for the financial support of this research project by the Eliteprogramme for Postdocs. S. Y. would like to thank the University of Tübingen for the financial support. The partial support by the Bulgarian NSF Grant No. KP-06-H28/7 and the networking support by the COST Actions, Grants No. CA16104 and No. CA16214, are also gratefully acknowledged. C. K. acknowledges support from the DFG research Grant No. 413873357.

[1] J. D. Bekenstein, Nonexistence of baryon number for static black holes, Phys. Rev. D **5**, 1239 (1972).
[2] A. E. Mayo and J. D. Bekenstein, No hair for spherical black holes: Charged and nonminimally coupled scalar field with self-interaction, Phys. Rev. D **54**, 5059 (1996).
[3] T. P. Sotiriou, Black holes and scalar fields, Classical Quantum Gravity **32**, 214002 (2015).
[4] T. P. Sotiriou and V. Faraoni, Black Holes in Scalar-Tensor Gravity, Phys. Rev. Lett. **108**, 081103 (2012).
[5] C. A. R. Herdeiro and E. Radu, Asymptotically flat black holes with scalar hair: A review, Int. J. Mod. Phys. D **24**, 1542014 (2015).
[6] C. A. R. Herdeiro and E. Radu, Kerr Black Holes with Scalar Hair, Phys. Rev. Lett. **112**, 221101 (2014).
[7] Y.-Q. Wang, Y.-X. Liu, and S.-W. Wei, Excited kerr black holes with scalar hair, Phys. Rev. D **99**, 064036 (2019).
[8] J. F. Delgado, C. A. Herdeiro, and E. Radu, Kerr black holes with synchronised scalar hair and higher azimuthal harmonic index, Phys. Lett. B **792**, 436 (2019).
[9] J. F. Delgado, C. A. Herdeiro, E. Radu, and H. Runarsson, Kerr-newman black holes with scalar hair, Phys. Lett. B **761**, 234 (2016).
[10] C. A. R. Herdeiro, E. Radu, and H. Rúnarsson, Kerr black holes with self-interacting scalar hair: Hairier but not heavier, Phys. Rev. D **92**, 084059 (2015).
[11] C. Herdeiro, E. Radu, and H. Rúnarsson, Kerr black holes with proca hair, Classical Quantum Gravity **33**, 154001 (2016).
[12] N. M. Santos, C. L. Benone, L. C. Crispino, C. A. Herdeiro, and E. Radu, Black holes with synchronised Proca hair: Linear clouds and fundamental non-linear solutions, J. High Energy Phys. 07 (2020) 010.
[13] J. Kunz, I. Perapechka, and Y. Shnir, Kerr black holes with parity-odd scalar hair, Phys. Rev. D **100**, 064032 (2019).
[14] J. Kunz, I. Perapechka, and Y. Shnir, Kerr black holes with synchronised scalar hair and boson stars in the Einstein-Friedberg-Lee-Sirlin model, J. High Energy Phys. 07 (2019) 109.
[15] L. G. Collodel, D. D. Doneva, and S. S. Yazadjiev, Rotating tensor-multiscalar black holes with two scalars, Phys. Rev. D **102**, 084032 (2020).
[16] Z.-K. Guo, N. Ohta, and T. Torii, Black holes in the dilatonic Einstein-Gauss-Bonnet theory in various dimensions. I. Asymptotically flat black holes, Prog. Theor. Phys. **120**, 581 (2008).
[17] B.-H. Lee, W. Lee, and D. Ro, Expanded evasion of the black hole no-hair theorem in dilatonic Einstein-Gauss-Bonnet theory, Phys. Rev. D **99**, 024002 (2019).
[18] G. A. Gonzalez, B. Kleihaus, J. Kunz, and S. Mojica, Innermost stable circular orbits of neutron stars in dilatonic-Einstein-Gauss-Bonnet theory, Phys. Rev. D **99**, 024041 (2019).
[19] P. V. Cunha, C. A. R. Herdeiro, B. Kleihaus, J. Kunz, and E. Radu, Shadows of Einstein–dilaton–Gauss–Bonnet black holes, Phys. Lett. B **768**, 373 (2017).
[20] J. L. Blazquez-Salcedo, F. S. Khoo, and J. Kunz, Quasinormal modes of Einstein-Gauss-Bonnet-dilaton black holes, Phys. Rev. D **96**, 064008 (2017).
[21] D. D. Doneva and S. S. Yazadjiev, New Gauss-Bonnet Black Holes with Curvature-Induced Scalarization in Extended Scalar-Tensor Theories, Phys. Rev. Lett. **120**, 131103 (2018).
[22] H. O. Silva, J. Sakstein, L. Gualtieri, T. P. Sotiriou, and E. Berti, Spontaneous Scalarization of Black Holes and Compact Stars from a Gauss-Bonnet Coupling, Phys. Rev. Lett. **120**, 131104 (2018).
[23] G. Antoniou, A. Bakopoulos, and P. Kanti, Evasion of No-Hair Theorems and Novel Black-Hole Solutions in Gauss-Bonnet Theories, Phys. Rev. Lett. **120**, 131102 (2018).
[24] G. Antoniou, A. Bakopoulos, and P. Kanti, Black-hole solutions with scalar hair in Einstein-scalar-Gauss-Bonnet theories, Phys. Rev. D **97**, 084037 (2018).
[25] M. Minamitsuji and T. Ikeda, Scalarized black holes in the presence of the coupling to Gauss-Bonnet gravity, Phys. Rev. D **99**, 044017 (2019).
[26] H. O. Silva, C. F. B. Macedo, T. P. Sotiriou, L. Gualtieri, J. Sakstein, and E. Berti, Stability of scalarized black hole solutions in scalar-gauss-bonnet gravity, Phys. Rev. D **99**, 064011 (2019).
[27] A. Bakopoulos, G. Antoniou, and P. Kanti, Novel black-hole solutions in Einstein-scalar-Gauss-Bonnet theories with a cosmological constant, Phys. Rev. D **99**, 064003 (2019).
[28] D. D. Doneva, K. V. Staykov, and S. S. Yazadjiev, Gauss-Bonnet black holes with a massive scalar field, Phys. Rev. D **99**, 104045 (2019).
[29] C. F. B. Macedo, J. Sakstein, E. Berti, L. Gualtieri, H. O. Silva, and T. P. Sotiriou, Self-interactions and spontaneous black hole scalarization, Phys. Rev. D **99**, 104041 (2019).
[30] D. D. Doneva, S. Kiorpelidi, P. G. Nedkova, E. Papantonopoulos, and S. S. Yazadjiev, Charged Gauss-Bonnet black holes with curvature induced scalarization in the extended scalar-tensor theories, Phys. Rev. D **98**, 104056 (2018).

[31] G. Antoniou, A. Bakopoulos, P. Kanti, B. Kleihaus, and J. Kunz, Novel Einstein–scalar-Gauss-Bonnet wormholes without exotic matter, Phys. Rev. D **101**, 024033 (2020).
[32] J. L. Blazquez-Salcedo, D. D. Doneva, J. Kunz, and S. S. Yazadjiev, Radial perturbations of the scalarized Einstein-Gauss-Bonnet black holes, Phys. Rev. D **98**, 084011 (2018).
[33] J. L. Blazquez-Salcedo, D. D. Doneva, S. Kahlen, J. Kunz, P. Nedkova, and S. S. Yazadjiev, Axial perturbations of the scalarized Einstein-Gauss-Bonnet black holes, Phys. Rev. D **101**, 104006 (2020).
[34] J. L. Blazquez-Salcedo, D. D. Doneva, S. Kahlen, J. Kunz, P. Nedkova, and S. S. Yazadjiev, Polar quasinormal modes of the scalarized Einstein-Gauss-Bonnet black holes, Phys. Rev. D **102**, 024086 (2020).
[35] D. D. Doneva, K. V. Staykov, S. S. Yazadjiev, and R. Z. Zheleva, Multiscalar Gauss-Bonnet gravity: Hairy black holes and scalarization, Phys. Rev. D **102**, 064042 (2020).
[36] D. D. Doneva and S. S. Yazadjiev, Neutron star solutions with curvature induced scalarization in the extended Gauss-Bonnet scalar-tensor theories, J. Cosmol. Astropart. Phys. 04 (2018) 011.
[37] B. Kleihaus, J. Kunz, and P. Kanti, Particle-like ultracompact objects in Einstein-Scalar-Gauss-Bonnet theories, Phys. Lett. B **804**, 135401 (2020).
[38] B. Kleihaus, J. Kunz, and P. Kanti, Properties of ultracompact particlelike solutions in Einstein-scalar-Gauss-Bonnet theories, Phys. Rev. D **102**, 024070 (2020).
[39] P. V. P. Cunha, C. A. R. Herdeiro, and E. Radu, Spontaneously Scalarized Kerr Black Holes in Extended Scalar-Tensor–Gauss-Bonnet Gravity, Phys. Rev. Lett. **123**, 011101 (2019).
[40] L. G. Collodel, B. Kleihaus, J. Kunz, and E. Berti, Spinning and excited black holes in Einstein-scalar-Gauss–Bonnet theory, Classical Quantum Gravity **37**, 075018 (2020).
[41] A. Dima, E. Barausse, N. Franchini, and T. P. Sotiriou, Spin-induced black hole spontaneous scalarization, arXiv:2006.03095.
[42] S. Hod, Onset of spontaneous scalarization in spinning gauss-bonnet black holes, arXiv:2006.09399.
[43] A. Dima and E. Barausse, Numerical investigation of plasma-driven superradiant instabilities, Classical Quantum Gravity **37**, 175006 (2020).
[44] I. Racz and G. Z. Toth, Numerical investigation of the late-time Kerr tails, Classical Quantum Gravity **28**, 195003 (2011).
[45] K. H. Lockitch and J. L. Friedman, Where are the R-modes of isentropic stars?, Astrophys. J. **521**, 764 (1999).
[46] J. Ruoff, A. Stavridis, and K. D. Kokkotas, Inertial modes of slowly rotating relativistic stars in the Cowling approximation, Mon. Not. R. Astron. Soc. **339**, 1170 (2003).
[47] Y.-X. Gao, Y. Huang, and D.-J. Liu, Scalar perturbations on the background of Kerr black holes in the quadratic dynamical Chern-Simons gravity, Phys. Rev. D **99**, 044020 (2019).
[48] W. Krivan, P. Laguna, and P. Papadopoulos, Dynamics of scalar fields in the background of rotating black holes, Phys. Rev. D **54**, 4728 (1996).
[49] W. Krivan, P. Laguna, P. Papadopoulos, and N. Andersson, Dynamics of perturbations of rotating black holes, Phys. Rev. D **56**, 3395 (1997).
[50] A. Zenginoglu, Hyperboloidal layers for hyperbolic equations on unbounded domains, J. Comput. Phys. **230**, 2286 (2011).
[51] E. Harms, S. Bernuzzi, and B. Brügmann, Numerical solution of the 2 + 1 Teukolsky equation on a hyperboloidal and horizon penetrating foliation of Kerr and application to late-time decays, Classical Quantum Gravity **30**, 115013 (2013).
[52] E. Harms, S. Bernuzzi, A. Nagar, and A. Zenginoglu, A new gravitational wave generation algorithm for particle perturbations of the Kerr spacetime, Classical Quantum Gravity **31**, 245004 (2014).
[53] C. J. Krüger and K. D. Kokkotas, Fast Rotating Relativistic Stars: Spectra and Stability without Approximation, Phys. Rev. Lett. **125**, 111106 (2020).
[54] C. J. Krüger and K. D. Kokkotas, Dynamics of fast rotating neutron stars: An approach in the Hilbert gauge, Phys. Rev. D **102**, 064026 (2020).
[55] A. Sommerfeld, *Partial Differential Equations in Physics* (Academic Press, New York, 1949).
[56] J. Ruoff, The numerical evolution of neutron star oscillations, Ph.D thesis, Eberhard Karls Universität Tübingen, 2000.
[57] E. Berti, V. Cardoso, and A. O. Starinets, Quasinormal modes of black holes and black branes, Classical Quantum Gravity **26**, 163001 (2009).
[58] E. Berti, V. Cardoso, and C. M. Will, On gravitational-wave spectroscopy of massive black holes with the space interferometer LISA, Phys. Rev. D **73**, 064030 (2006).